

RESEARCH ARTICLE

10.1029/2017JB015404

Key Points:

- Fine-scale upper crustal structures of V_p , V_s , and V_p/V_s , together with earthquake locations near the Xinfengjiang reservoir, are obtained
- Focal mechanisms of 136 M1.5 or larger earthquakes are inverted
- Water may play important role in fault extension and earthquake mechanism change

Correspondence to:

X. Sun,
xsun@gig.ac.cn

Citation:

He, L., Sun, X., Yang, H., Qin, J., Shen, Y., & Ye, X. (2018). Upper crustal structure and earthquake mechanism in the Xinfengjiang Water Reservoir, Guangdong, China. *Journal of Geophysical Research: Solid Earth*, 123. <https://doi.org/10.1029/2017JB015404>

Received 26 DEC 2017

Accepted 10 APR 2018

Accepted article online 19 APR 2018

Upper Crustal Structure and Earthquake Mechanism in the Xinfengjiang Water Reservoir, Guangdong, China

Lipeng He^{1,2}, Xinlei Sun¹ , Hongfeng Yang³ , Jialing Qin^{1,2}, Yusong Shen⁴, and Xiuwei Ye⁴

¹State Key Laboratory of Isotope Geochemistry, Guangzhou Institute of Geochemistry, Chinese Academy of Sciences, Guangzhou, China, ²College of Earth and Planetary Sciences, University of Chinese Academy of Sciences, Beijing, China, ³Earth System Science Programme, Chinese University of Hong Kong, Hong Kong, ⁴Guangdong Earthquake Agency, Guangzhou, China

Abstract The Xinfengjiang Water Reservoir (XWR) in Guangdong, China, is one of the reservoirs that have triggered earthquakes of magnitudes greater than 6. Numerous earthquakes have occurred since the impoundment of the reservoir, making it one of the most active seismic zones in Guangdong. However, due to the lack of seismic stations, the detailed seismic structures and earthquake mechanisms within XWR have not been resolved, and the significance of XWR as a typical protracted earthquake location is not well judged. In this study, by collecting waveform data from both permanent and temporary stations from 2012 to 2015, we relocated 1,528 earthquakes and inverted both V_p and V_s structures from traveltimes of these earthquakes. Using waveform data, we also investigated focal mechanisms of earthquakes with magnitude greater than 1.5 in this region. Our results reveal fine crustal structure that has never been shown before and show complicated crust structure with several low-velocity zones extending to 5–10 km depth under the major faults. Earthquake focal mechanisms show more dip-slip faults than strike-slip faults, and the two types of earthquakes are roughly divided by the reservoir boundary. The direction of principle stress of the earthquakes is northwest-southeast, consistent with the direction of tectonic principal stress. Combining the above results, and investigation of historical earthquakes and water level change, we suggest that water loading cycle and diffusion play important role in XWR seismicity. They increase the pore pressure, make the earthquakes migrate to deeper depth, and change the type of earthquakes.

1. Introduction

The Xinfengjiang Water Reservoir (XWR) is one of the largest reservoirs in south China. It is located on the northwest of Heyuan, Guangdong province (Figure 1). Previously, there were few earthquakes in this area, but shortly after the initial impoundment of the reservoir in 1959, seismicity in XWR increased significantly (Ding et al., 1982; Guo et al., 2004). A magnitude 6.1 earthquake occurred on 19 March 1962 and became one of the largest reservoir-induced earthquakes in the world (Ding et al., 1983; Gupta, 2002; Talwani, 1997). Since then, numerous small earthquakes have occurred, including more than 50 earthquakes with magnitude greater than 4.0.

As one of the four reservoirs that have triggered earthquake with magnitude greater than 6, XWR provides a valuable opportunity for us to understand earthquake mechanisms and their relationship with deep structure and water level. Indeed, a series of investigations have been conducted on velocity structures, earthquake focal mechanism, and crustal deformation near the XWR. However, data from these studies are recorded from relatively few stations, and the focal mechanisms of the earthquakes and fine crustal structures are not well resolved. As such, the distribution and mechanism of the long-lasting seismicity since the inception of the reservoir remain poorly understood.

1.1. Geological Setting

The XWR area consists of Yanshanian granitic blocks that intruded into the Paleozoic and Mesozoic sedimentary rocks. To its east, a Late Cretaceous-Tertiary basin is separated from the block by a series of NNE faults (Ding et al., 1983). There are three major faults crossing this area in NNW, NNE, and NEE directions (Figure 1; Ding et al., 1983; Pan & Xiao, 1982; Yang et al., 2013). The NNE fault systems include Heyuan fault (HYF), Renzhishi fault (RZSF), and Daping-Yanqian fault (DYF). They are mostly developed near the ground and located in and around the reservoir and are mainly reverse faults. The 1962 M6.1 earthquake occurred

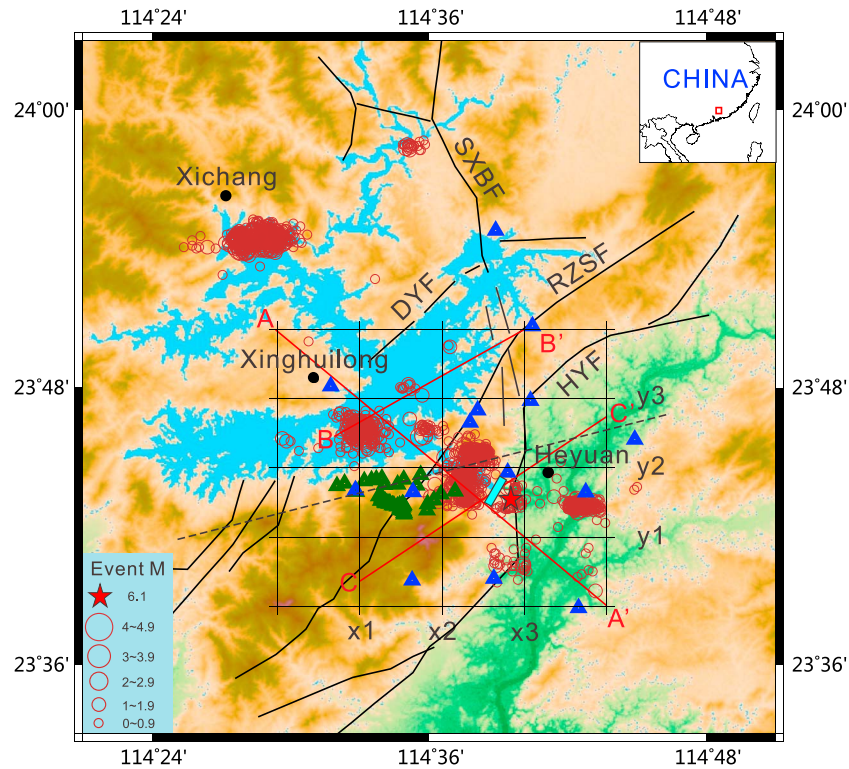


Figure 1. Geological map of the Xinfengjiang Water Reservoir (XWR). Inserted map shows the location of XWR (red square). Faults are plotted using solid or dashed (inferred fault) lines. The NNE and NNW fault systems include Heyuan faults (HYF), Renzhishi faults (RZSF), Daping-Yanqian faults (DYF), and Shijiao-Xinggong-Baitian faults (SXBF). Red circles are earthquakes with $M > 0$ from 2012 to 2015, and blue and green triangles are permanent and temporary seismic stations used in this study, respectively. The reservoir dam (cyan rectangle), the main shock in 1962 (red star), and a series of cross-section locations ($y_1, y_2, y_3, x_1, x_2, x_3, AA', BB',$ and CC') are also plotted. Note that profile AA' is approximately perpendicular to the NNE faults system, and BB' and CC' are in northeast direction, which is perpendicular to NNE faults.

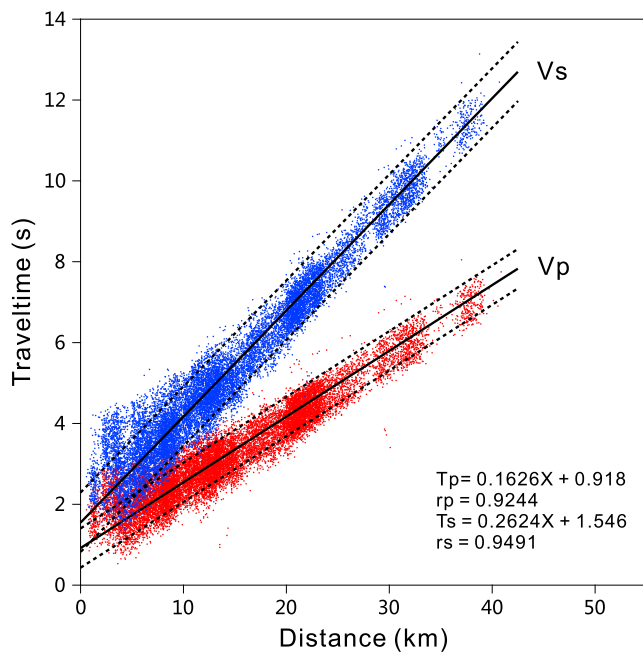


Figure 2. P and S wave travel times relative to distance. Red dots represent P wave travel times, and blue dots represent S wave travel times. Two black straight lines are least squares linear fit for P and S wave travel times.

near the dam, beside the HYF. The NNW faults locate in the reservoir and consist of multiple segments, in which the Shijiao-Xinggong-Baitian faults (SXBF) are the dominant ones. These faults are strike-slip faults and cut across other faults. The NEE fault system does not show much surficial signature, but geological and gravity surveys show that it cuts deep into crust beneath the XWR and divides the area into two blocks (Ding et al., 1983). These faults intersect with each other and define the frame of the geological structures in XWR area. However, not all the faults are associated with active seismicity and the faulting types remain elusive. For example, the majority of the earthquakes in the XWR area is located near the dam, by the HYF area, or in the northwest of the reservoir near Xichang (Figure 1). It is difficult to judge from locations alone which fault system is related to earthquakes.

1.2. Previous Studies

Efforts have been made to resolve the velocity structure of XWR. Guo and Feng (1992) jointly inverted earthquake location and 3-D velocity structure in this area and found a correlation of low-velocity structure with the gravity and magnetism anomalies in depth. However, the data they used are only from eight seismic stations; thus, the resolution of their results is quite limited, especially at shallow depth. With more temporary stations deployed, Yang et al. (2013) obtained a 3-D velocity structure with high- and low-velocity zones cutting across each other. After the occurrence of 2012 M4.8 earthquake in the northwest corner of XWR, Ye et al. (2013)

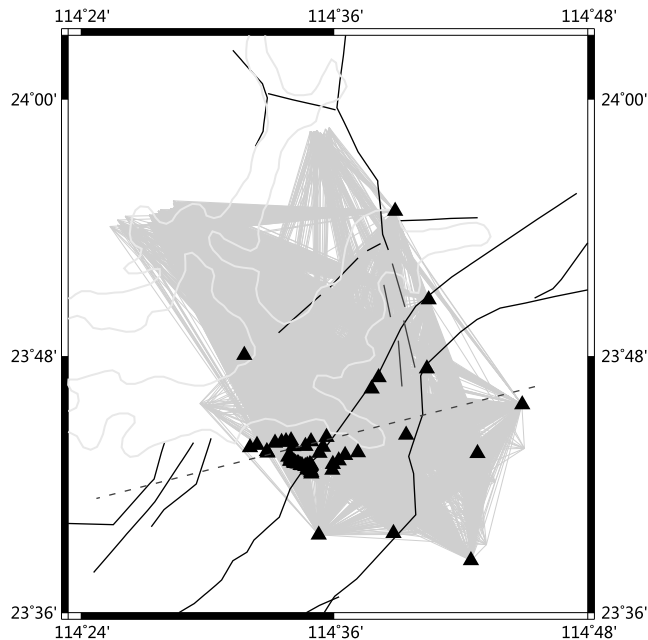


Figure 3. *P* wave raypath coverage in this study. Gray lines represent earthquake-station pairs. Black triangles are stations used in this study. *S* wave coverage is the same as *P* wave.

inverted both earthquake location and crustal structures in that area. Their results show a high-velocity block at about 10 km, and they found that aftershocks of the M4.8 earthquakes cut across this high-velocity block. Although these studies show some main characteristics of the structures in the whole area, due to the scarcity of seismic stations, especially permanent stations in XWR, they did not resolve the detailed structures. Fine features such as fault location, geometry, velocity changes, and their relationship with seismicity still need further investigation.

Various studies generally agreed that earthquakes in XWR are mainly controlled by local tectonic stress, although there are controversies as how the tectonic stress is distributed and which fault systems are the main control faults (Cheng et al., 2012; Ding et al., 1982; Shen et al., 1974; Wang et al., 1976; Wei et al., 1991). On the other hand, it has been proposed that earthquakes in XWR are correlated with water impoundment at shallow depth (Guo et al., 2004; Pan & Xiao, 1982). Analysis of earthquake focal mechanisms in XWR pointed out that after the M6.1 earthquake, the dominated earthquakes have changed from strike slip to dip slip (Ding et al., 1982; Wang et al., 1976). However, it is not clear why the earthquake type has changed, and we need more evidence to test this time-changing phenomenon.

In this study, we use earthquake waveform data recorded by the newly installed Xingfengjiang seismic network and a temporary network consisting of 42 stations, to jointly invert the earthquake location and 3-D crustal structures in XWR area. Our results reveal fine structures that have never been obtained before and show their correlation with location and mechanisms of clustered earthquakes.

2. Data and Method

In order to monitor earthquakes near the XWR, the Guangdong Earthquake Agency has deployed 14 permanent broadband seismographs around the XWR since 2012. The stations are located in granitic basement, equipped with 60 or 120-s to 50-Hz broadband sensors and at least 24-bit digital acquisition systems. To complement the permanent network and to investigate the fine structure of the RZSF southwest of the reservoir, we deployed a temporary seismic network consisting of 42 short-period (0.2–120-Hz) seismometers (Figure 1). They are deployed from January to February 2015, with a mean interstation distance of 100–500 m.

We systematically examined earthquakes near the XWR from 2012 to 2015. Because the earthquake-station distance is small (≤ 40 km), we chose earthquakes with magnitude greater than 0 from earthquake catalog of Guangdong Earthquake Agency. Based on waveform quality, a total of 1,507 earthquakes for the permanent Xingfengjiang network stations and 189 earthquakes for the temporary network station were finally selected. We then handpicked both *P* and *S* wave arrivals for each event. In this process, we first applied a two-pole Butterworth band-pass filter between 1 and 15 Hz to the seismograms and then visually inspected *P* and *S* arrivals. When picking the *P* and *S* arrivals, we checked three components of the seismic data simultaneously. *P* waves with sharp and clear onsets, especially on vertical component, were chosen. Picking *S* wave arrivals were a little complicated. We first marked the predicted *S* arrivals using an average south China velocity model (Zhou et al., 2012) then aligned the data according to their distances for each earthquake. Waveforms that fall

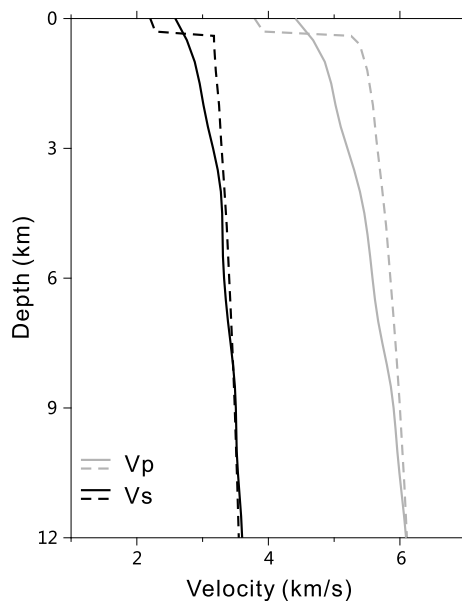


Figure 4. One-dimensional *P* wave and *S* wave velocity in XWR area. Black and gray lines are for *P* and *S* wave velocities, respectively. Dashed lines are initial velocity models from Zhou et al. (2012), and solid lines are averaged one-dimensional velocity model from our final inversion results.

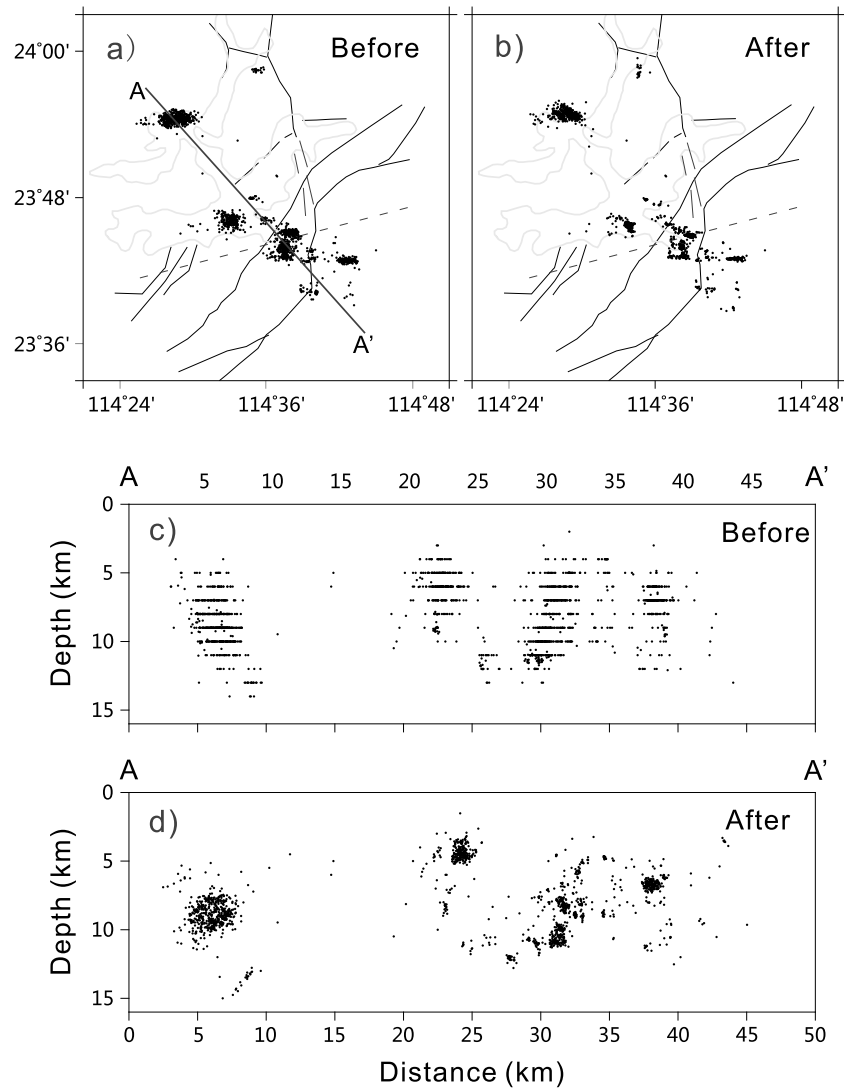


Figure 5. Map views of earthquake (black dots) location (a) before and (b) after relocation process and (c and d) cross sections (with position plotted in [a]) of earthquake location before and after relocation. After relocation, the depth distribution of the earthquakes improved a lot.

within 1-s time window of predictions, or with clear phases and are consistently moving out with distance, were picked as *S* waves.

All the picked data were further processed to ensure the data quality and coverage for both *P* and *S* waves. First, for each earthquake, we checked the data distribution and chose those that were recorded by five or more stations for both *P* and *S* waves. Earthquakes that only have *P* or *S* arrival picks were discarded, for better comparison between V_p and V_s and to ensure the reliability of V_p/V_s ratio (Zhang, 2003). We then plotted all the *P* and *S* travel times according to distance and fitted the data with least squares linear trend (Figure 2). The outliers that fall outside two standard deviations of the data were eliminated. Finally, we collected 19,917 *P* and *S* arrival times. Raypaths of the data are shown in Figure 3.

We combine HypoDD (Waldhauser & Ellsworth, 2000) and fast marching tomography (Rawlinson et al., 2006; Sethian, 2001) to relocate earthquakes and to invert both V_p and V_s velocities. Fast marching tomography uses a grid-based eikonal solver (fast marching method) to trace wavefronts in 3-D complex structures thus can effectively calculate travel times in our study. It also uses nonlinear searching scheme to find the best model space. Our relocation and tomography inversion follow the paper of Waldhauser and Ellsworth (2000) and Rawlinson et al. (2006), in which details can be found.

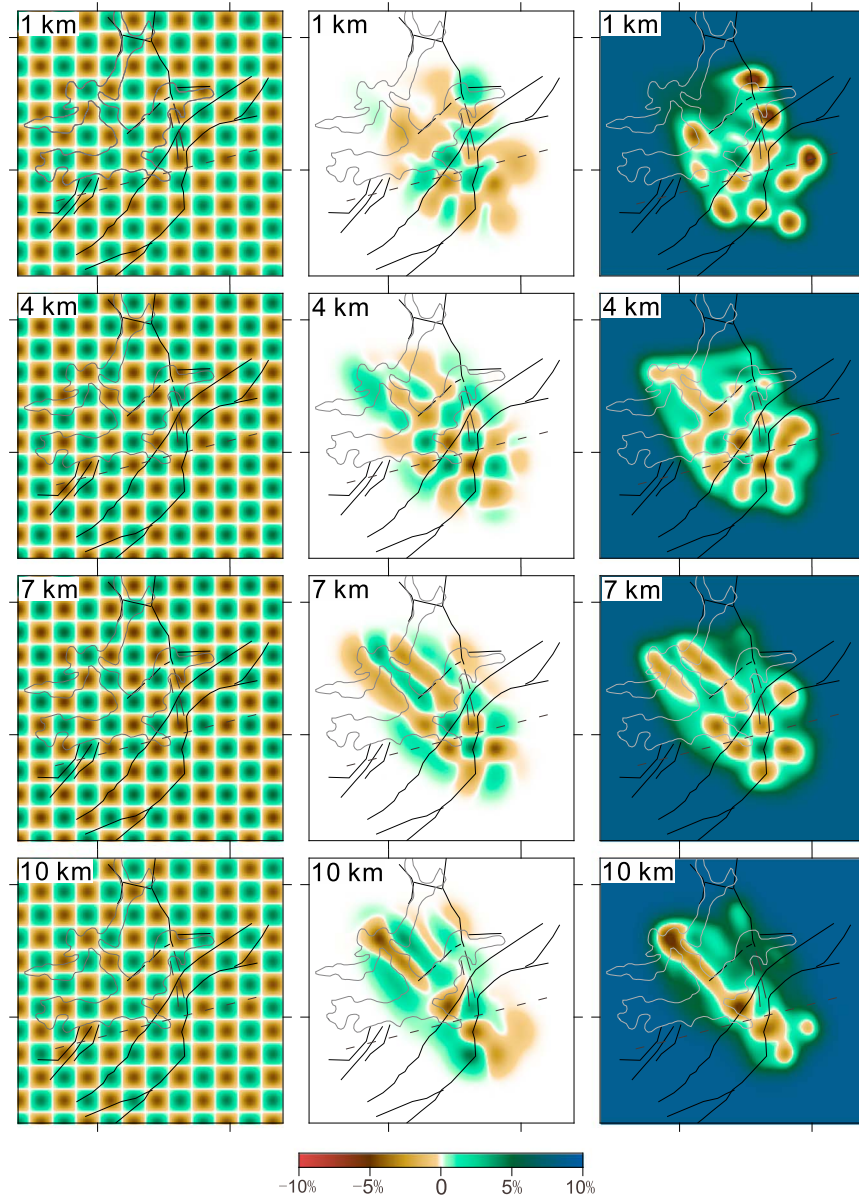


Figure 6. Map view of checkerboard test. (left column) Input model. It is generated by perturbing the reference model with $\pm 10\%$ velocity variation in alternate grids; (center column) the recovered velocity at depth of 1, 4, 7, and 10 km, respectively. In this test, the starting model is the same as the reference model. (right column) Same as in the center column, but the initial model in inversion has 0.5 km/s velocity increase compared to the reference model. The recovered velocity models from both columns are generally the same and show very good resolution at depths of 1, 4, and 7 km.

In the inversion, we first relocate earthquakes using a 1-D reference velocity model of south China (Figure 4; Zhou et al., 2012). The maximum distance between event pair and stations is set to be 40 km, and the minimal common record number required to define a neighbor is set to be 8. Then we use the new earthquake locations to invert both V_p and V_s structures. The resulted 3-D velocities are averaged as new 1-D reference model to relocate earthquakes again, and new inversion of V_p and V_s are done using the new earthquake locations. After each iteration, we calculate the RMS of the data, and if the RMS does not change much compared to previous iteration, it is considered to be converged. Generally, the RMS of the data will not change much after third iteration, but for simplicity, we always iterate six times to get the final result. Considering the data quality, we use different weight for P and S arrivals (0.8 and 0.2, respectively) in the relocation process.

The tomographic region is ~ 25 km long, 22 km wide, and 15 km in depth from the ground surface. In the parameterization, we set the control grid to be about 2 km apart in all three dimensions. We also set the

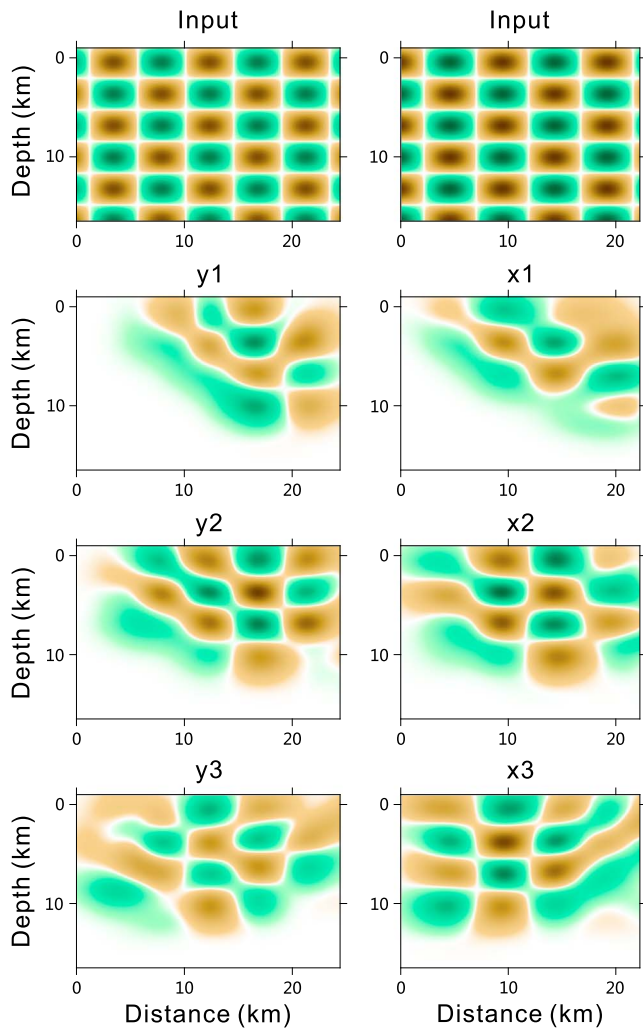


Figure 7. Cross-section images of resolution test result. The position of the cross section can be found in Figure 1. Recovery is generally quite good above 10-km depth. Because of the poor ray coverage at SW corner of study area (see Figures 1 and 4), cross sections y1, y2, and x1 have poor resolution in that area.

upper and lower bounds in depth at -1 km (above horizon) and 16 km in order to account for the boundary effect. Water layer is not included in our model, because all the seismic rays do not transverse water layer in our earthquake-station distribution.

Velocities are calculated using cubic B-spline, which generates a smoothly varying model. We vary different damping (range from 0.1 to 10) and smoothing parameters (range from 0.1 to 10) in the inversion, and the final choice of these parameters (1 and 0.5, respectively) is determined in the synthetic test, based on the RMS between input and output models.

3. Earthquake Relocation Results

A total of 1,528 earthquakes have been relocated in our study area (Figure 5). Earthquakes are located mostly near the dam and in the northwest of the reservoir near Xichang. There is no significant change in the horizontal view of these earthquakes after relocation. However, cross section along the northwest direction shows significant improvement in location after relocation: scattered earthquakes are clustered in four groups. Earthquakes near DYF are generally at shallow depth of about 5 km, and the other two groups near HYF and the dam spread from 5 to 10 km, with the group to the east of HYF showing a northwest dip direction. Moreover, earthquakes in northwest group are clustered at around 10 km, although they are somehow scattered.

4. Three-Dimensional V_p and V_s Velocity Structure

4.1. Synthetic Test

We conduct checkerboard test to check the inversion resolution of the V_p and V_s models. The reference model is the average south China model (Zhou et al., 2012) as mentioned above. In the input model, the reference model is perturbed by $\pm 10\%$ for V_p and V_s in alternate control grids. We use fast marching method to generate synthetic travel time data for the same source-receiver geometry as observed. In the test, we also add travel time noise (0.05 s for P wave and 0.1 s for S wave) in our synthetic data. In order to test the starting model effect, we choose two starting models, one is the reference mode, and another is a model with 0.5 km/s higher P/S velocity in all depths compared to the starting model.

The recovered models for P waves are shown in Figures 6 and 7. S wave results are very similar as P wave because of the same ray coverage. The left column of Figure 6 is the input model. The central and right columns are recovered models from different starting models, with the reference model in the central and perturbed reference model in the right column. Our tests from both starting models show good resolution in most of the study area, indicating that initial velocity model has little effect on our results. In depth range, good resolutions are shown at 1 km, 4 km, and 7 km (white color means no velocity change). Because of scarcity of earthquakes below 10 km (Figure 5), the resolution at 10 km depth is relatively poor. We notice that although the test result can recover the pattern of the velocity structure at 10-km depth, it overestimates the variation amplitude by about 7%. This may affect the true result and shall be discussed later. Figure 7 shows resolution test results of six cross sections (positions are shown in Figure 1). The cross sections generally show good resolution in depth range in this area, except at the southwest corner of our study area (left side of x1 and y1), where the data coverage is poor (Figure 4).

4.2. V_p , V_s , and V_p/V_s Structure

Figure 8 shows the residual statistics of P and S travel times before and after inversion. There is a significant improvement in data misfit, indicating that our earthquake location and velocity models are good.

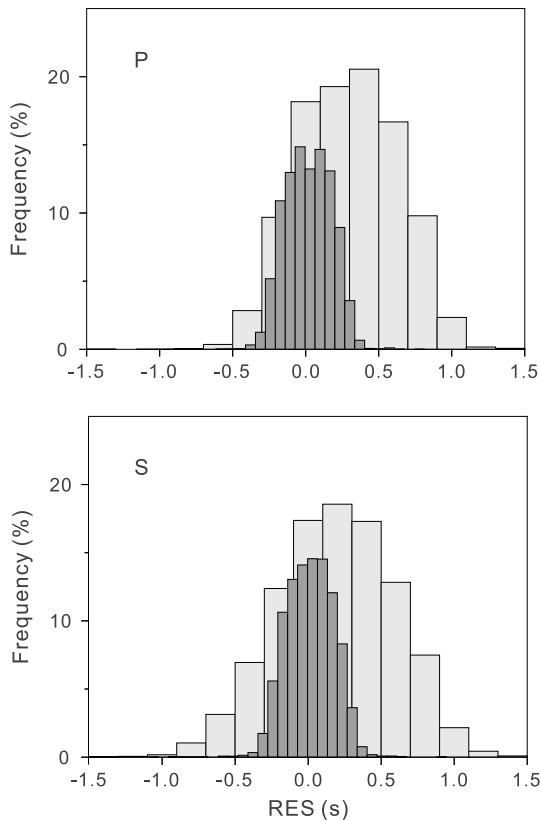


Figure 8. Travel time residual distribution before (gray bars) and after (black bars) inversion for P (top) and S (bottom) waves.

Figure 9 shows V_p (left), V_s (center), and V_p/V_s (right) maps at different depths. In general, our P wave and S wave velocity structures are very similar. At 1-km depth, low velocities spread widely across different faults such as DYF, RZSF, and HYF. The low V_p (3.5–5 km/s) and V_s (2–3 km/s) imply the presence of damaged fault zones at shallow depth. At 4-km depth, low-velocity structures shrink gradually to the southeast of HYF and northwest of DYF and RZSF. At 7-km depth, three low anomalies dominated, located in the northwest region near Xichang, in the southeast side near HYF, and near Xinhuilong between DYF and RZSF. The low-velocity region near HYF may reflect the existence of rift basin, and the low regions in the northwest part may indicate fault fractures in this area. At 10 km, although the resolution is not very good, low V_p and V_s are shown in the south part of the study area and roughly coincide with the inferred deep NEE faults (dashed line) from gravity anomaly. Based on the resolution test, the velocity at 10-km depth should be lower than in our result and should be no larger than 6.5 km/s. On the other hand, V_p/V_s ratios are low (≤ 1.6) in most of the areas at both shallow (≤ 4 km) and deep (≥ 7 km). However, at intermediate depth (between 4 and 7 km), there are two high V_p/V_s (≥ 1.8) blocks to the southeast of Xinhuilong and Xichang, where the obvious low V_s regions are located.

Figure 10 shows three cross sections of our P wave velocity (upper panel), S wave velocity (middle panel), and V_p/V_s (lower panel) models, with the cross-section locations shown in Figure 1. In these figures, black inverted triangles represent three faults at the surface (DYF, RZSF, and HYF), and black dots are projected earthquakes (within 2-km distance) to the cross section. Profile AA' is along NW-SE direction, similar to the NW faults system orientation. It cuts across the three NNE faults nearly perpendicularly. Below these NNE faults (black inverted triangles), there are three low-velocity regions extending from the surface to ~5 km depth, which suggest the existence of fracture zones. There is also a consistent low-velocity

and high V_p/V_s block at about 7 to 10-km depth from RZSF to HYF, indicating a deep fault along the reservoir gorge. BB' and CC' cross sections cut perpendicular to the NNW fault systems, one between DYF and RZSF and the other one cutting HYF. Underneath BB', there are two high-velocity blocks between 5 and 10-km depth, and in between them is a low-velocity block. CC' has two obvious low-velocity blocks beneath HYF. The upper low-velocity block extends from surface to about 5-km depth and may represent HYF. Another low-velocity block lies between 7 and 10 km, which is the projection of the deep fault along AA'. Our results show clearly that the three fault systems extend no deeper than 5 km in depth. The deep fault at 7–10-km depth in NW direction is a deep fault along the reservoir gorge. It cannot be seen from surface, but previous studies (e.g., Ding et al., 1983; Yang et al., 2013) suggested its existence. The current earthquake locations indicate that this fault may be the main fault at the southeast part of the XWR.

When we compare V_p and V_s to V_p/V_s , we notice that low/high V_p and V_s velocity regions generally show high/low V_p/V_s , although the anticorrelation of V_p and V_p/V_s is not as obvious as that of V_s and V_p/V_s (Figure 9). This anticorrelation is clear in most of the areas to the northwest side of HFY, where the reservoir is located. In the cross sections (Figure 10), high V_p/V_s and low V_s could be seen clearly beneath major faults at nearly all depth range.

The cross sections in Figure 10 show that most earthquakes are located at the boundary of low-velocity or high V_p/V_s regions, not in the central part of the structure. This may indicate that earthquakes are ruptured from the periphery of the fractured zone.

4.3. Interpretations

Velocity changes in fault areas are combined effects of lithology, crack density, porosity, pore pressure, and water content. Various studies have shown that seismic velocities in damaged fault zones can be 20–50% lower than the host rock (e.g., Aki & Lee, 1976; Nur & Simmons, 1969; Yang & Zhu, 2010; Yang

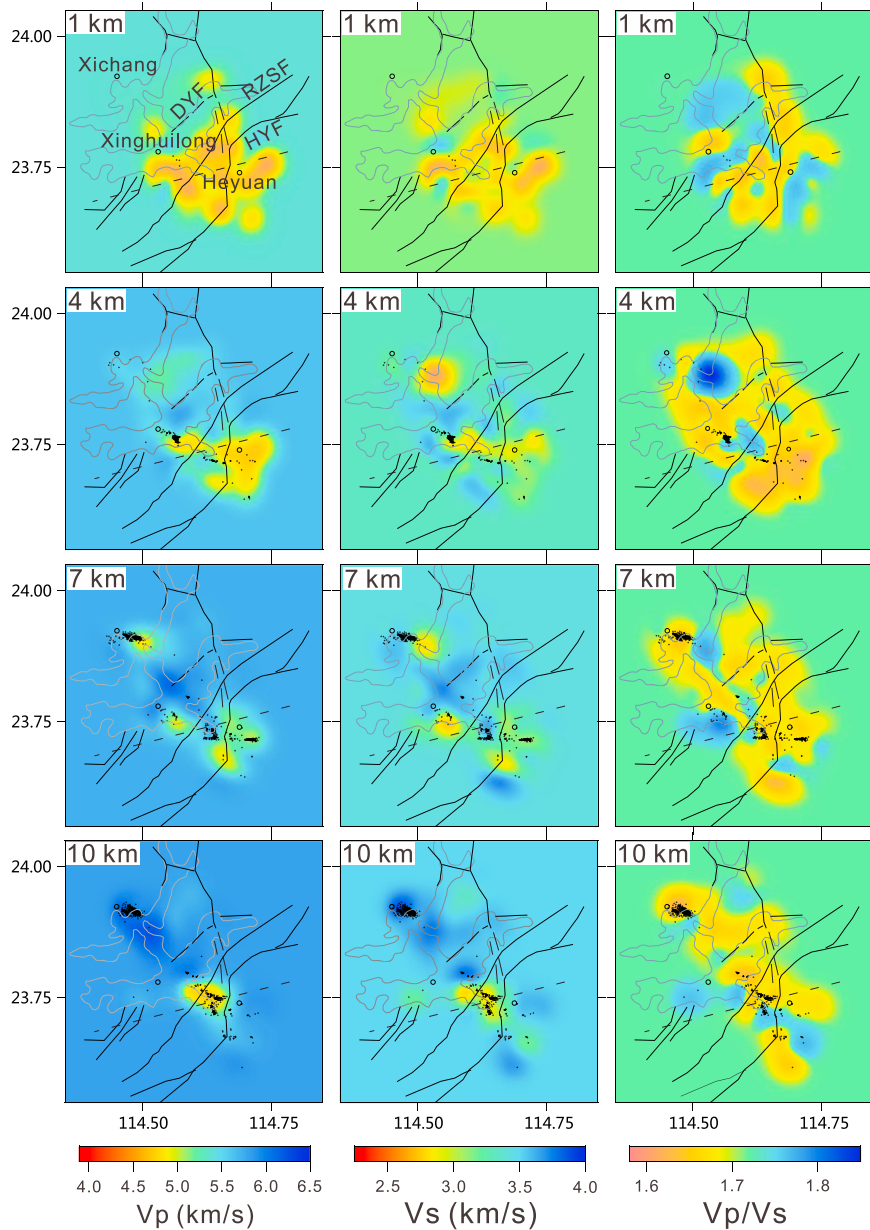


Figure 9. Map view of our velocity results at depths of 1, 4, 7, and 10 km, respectively. Left, central, and right columns are P wave velocity, S wave velocity, and V_p/V_s , respectively. Faults (black lines) are also plotted in the figures. Black dots are projected earthquakes within 2 km of the cross section.

et al., 2014; Yang, 2015). Although in dry rocks, fractures can reduce both V_p and V_s because of the decrease in shear modulus, water in fractures may increase the bulk modulus and thus increase V_p (Nur, 1972; Shearer, 1988). At the same time, because water has little effect on shear modulus, V_s remains almost unchanged. However, even the V_p and V_s change may be different in saturated rocks; V_p/V_s is very sensitive to water content. In water-saturated rocks, V_p/V_s generally increase for thin cracks and decrease for thick cracks (Nur & Simmons, 1969; Shearer, 1988). So with different combination of fractures, water content will generate different V_p , V_s , and V_p/V_s anomalies. One thing to notice here is that although V_p in water-saturated rock is higher than that in dry fractured rock, it may still be lower than V_p in intact rock.

Our results show low V_p/V_s at shallow depth but obvious high V_p/V_s in the main fault zones area in deeper depth (Figure 10). The low V_p/V_s at shallow depth may be because of open/thick cracks in granite.

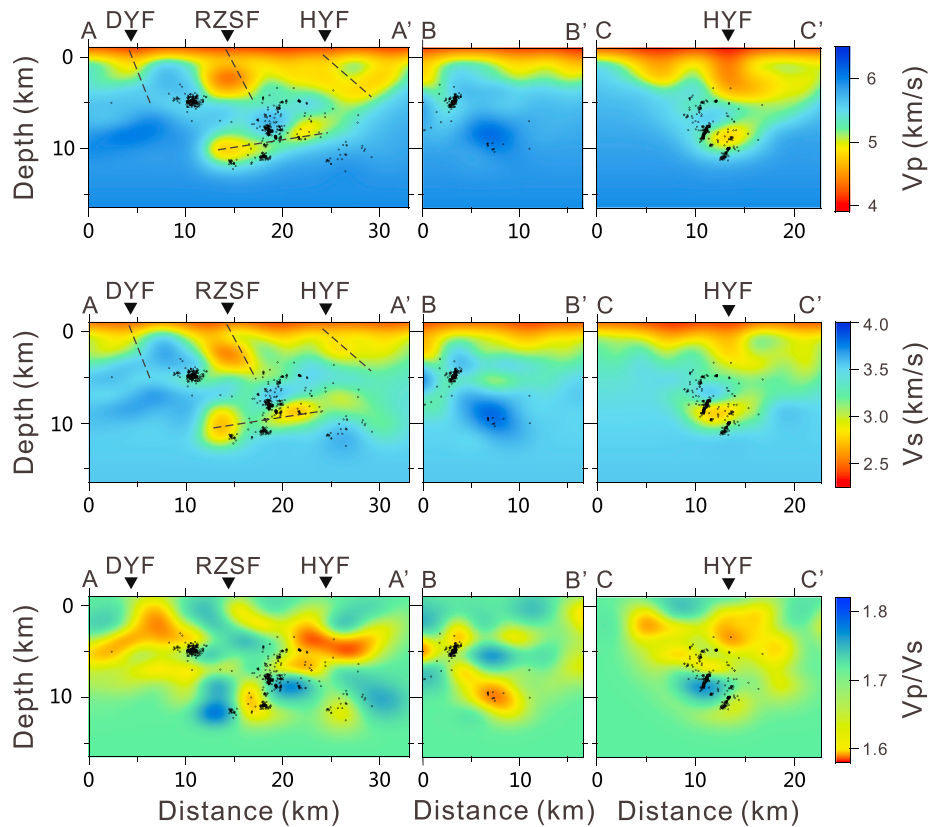


Figure 10. Cross sections along profile AA', BB', and CC' from left to right. Top, middle, and bottom panels show P wave velocity, S wave velocity, and V_p/V_s of the three cross sections. Black dots are projected earthquakes within 2 km of the cross section, and black triangles at the surface are faults. We also plotted the inferred subsurface location of the faults. Although we are not confident about the depth extent of the three NNE faults, they should not be deeper than 5 km.

However, when depth increases, increased confining pressure decreases the crack volume; as a result, the cracks become thinner, and V_p/V_s become higher.

On the other hand, the high V_p/V_s regions in our results also show low V_s and V_p anomalies (>1 km depth). The anticorrelation of V_p/V_s and V_s have been noticed previously in both saturated and dry rocks (Dixit et al., 2014; Gritto & Jarpe, 2014; Gritto et al., 2004; Moos & Zoback, 1983), suggesting the sensitivity of V_p/V_s to water content. However, relationship of V_p/V_s and V_p is not consistent. Both low V_p (e.g., Awad & Mizoue, 1995; Gupta, 2002; this study) and high V_p (Catchings et al., 2015; Dixit et al., 2014) exist at high V_p/V_s regions in different reservoir areas. The reasons may be related to different characteristics of the fractured rock, such as the aspect ratio, crack density, and degree of saturation, or it could also be related to different raypath sampling of P and S phases. Here in this study, we use almost identical P and S raypaths in our inversion process; thus, our calculation of V_p/V_s is more reliable.

It is also noticed that V_p/V_s exhibits decreased and increased values before and after main earthquakes ($M > 4$; Feng, 1977; Wang et al., 1976). Although our tomography result is only a snapshot of the postseismic stage in XWR area, the high V_p/V_s values in fault regions are consistent with these observations.

Combining the velocity structure, V_p/V_s , and earthquake locations before and after the reservoir impoundment, we suggest that water plays an important role in earthquake triggering: after impoundment of the reservoir, water begins to filter into the fractures. At this stage, water is not fully penetrated; thus, the opened fractures are dry and exhibit low V_p/V_s . After earthquakes, water continues penetrating in the opened fracture, increases the pore pressure, and extends the fractures to depth. As a result, the water-saturated rocks exhibit high V_p/V_s , and earthquake depths increase with time (more detailed discussion can be seen in section 6.1).

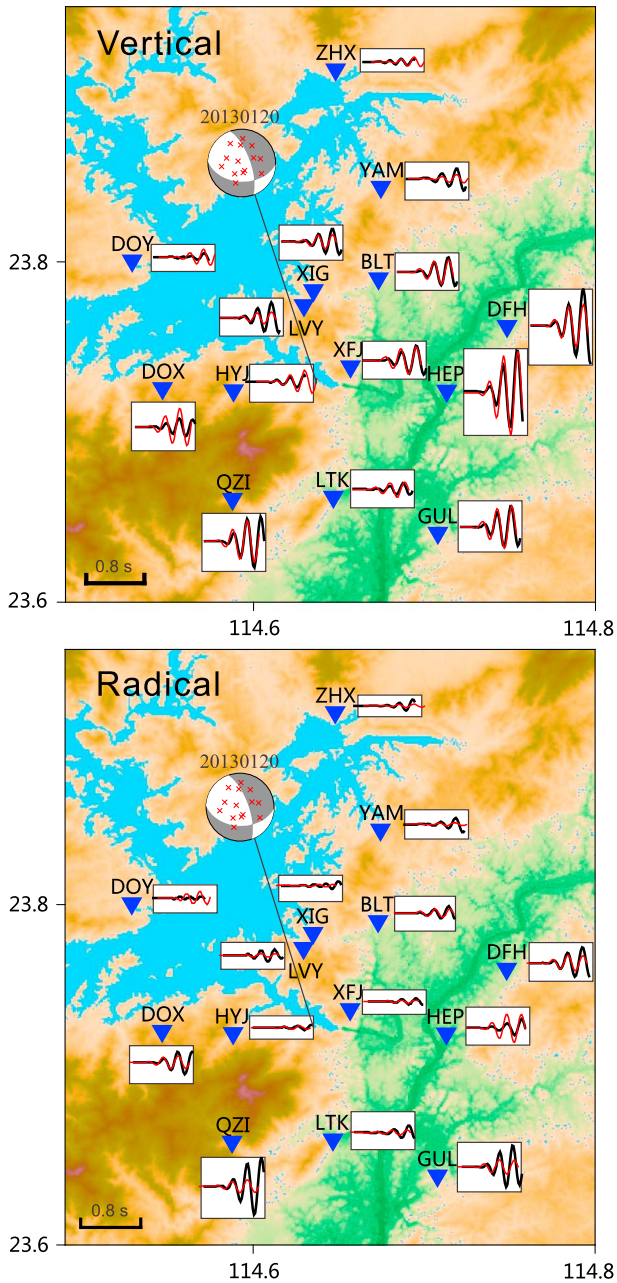


Figure 11. An example of focal mechanism inversion. The upper figure shows the vertical component, and the bottom figure shows the radial component seismograms. Observed (black lines) and synthetic (red lines) waveforms from our inversion model fit quite well. Mismatches of waveforms are from using 1-D averaged velocity model in XWR.

5. Earthquake Focal Mechanism

In this process, we choose earthquakes of magnitude greater than 1.5 in southeastern cluster of XWR. Earthquakes are also required to be recorded by more than eight stations with uniform azimuth coverage. Before the inversion, we rotated the original waveforms to great circle path and band-pass filtered the seismograms between 2 and 7 Hz. We first used *P* wave first motion to estimate the focal mechanism (Hardebeck & Shearer, 2002); then we used waveform data to further constrain the mechanism of each earthquake. In the waveform inversion, the gCAP method (Zhu & Ben-Zion, 2013; Zhu & Helmberger, 1996) was applied. Green's functions were generated from FK (Haskell, 1964; Zhu & Rivera, 2002) method, and the reference velocity model is the averaged 1-D model from our 3-D inversion result. Finally, a total of 136 focal mechanisms were obtained. Figure 11 shows an example of our focal mechanism inversion result. Synthetic waveforms (red) and observed waveforms (black) match quite well, despite the fact that one-dimensional model is used.

Twenty-nine representative focal mechanisms are plotted in Figure 12. The representative earthquakes are chosen from finer subgroup of earthquakes that have very similar mechanism, thus representing the general pattern of earthquake mechanisms in the area. Our results show that currently, the focal mechanisms in XWR area are dominated by dip-slip faults (~75%), followed by strike-slip faults (~20%). The dip-slip earthquakes are mainly distributed on the west side of the HYF, and the strike-slip faults are mainly located on the east side of the HYF.

The focal planes of these earthquakes generally show NNW/NEE orientation, which is consistent with the NNW/NNE fault systems in this area. Considering the depths of these earthquakes (mostly below 5-km depth), the deep NW faults are likely the corresponding fault planes. This is also supported by the distribution of earthquakes (Figure 1). From the results of our earthquake focal mechanisms, we calculated the principle stress direction (Vavryčuk, 2014) in XWR area. Our results show northwest/southeast horizontal compressional principal direction, which is consistent with most of previous studies (Ding et al., 1982; Guo & Feng, 1992; Huang & Yang, 2001). This result indicates that local stress is the major controlling factor in the XWR earthquakes.

It has been noticed that earthquake focal mechanisms in XWR area changed with time: before the M6.1 earthquake, earthquakes were dominated by strike-slip type; after that, earthquakes are dominated by dip-slip type (Ding et al., 1982; Guo et al., 2004; Wang et al., 1976; Zang, 1983). This strike-slip to dip-slip change cycle may have occurred several times with the occurrence of big earthquakes in XWR, but the lack of high-quality waveform data from the 1980s to 2000s prohibits detailed investigations. Our current focal mechanism results suggest that XWR area is now in the

protracted stage of big earthquakes, although we are not sure that it is due to the M6.1 earthquake or the later big earthquakes.

Earthquake focal mechanism change is the reflex of stress change in fault area. If the regional stress has the maximum and minimum stress direction both in horizontal direction, it is easy to generate strike-slip earthquakes, as the case in XWR before the M6.1 main shock. However, after the M6.1 main earthquake, horizontal stress decreases due to stress release. Meanwhile, the water load increases the stress much more in vertical direction than in horizontal direction (Zang, 1983). The vertical middle principal stress then may become the maximum stress and thus trigger a normal fault earthquake (Zang, 1983). Our

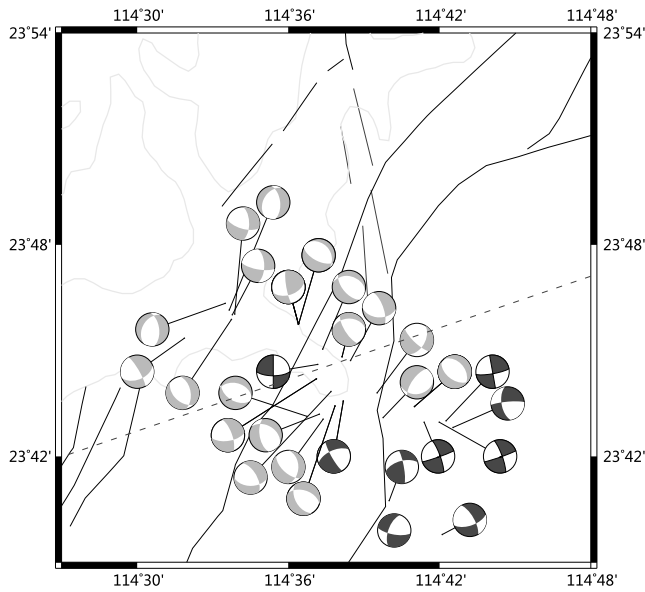


Figure 12. Focal mechanisms of 29 representative earthquakes. Most of the focal mechanisms are dip-strike faults (gray beach balls), but there are also some strike faults (black beach balls) in eastside of HYF.

observation of dip-slip earthquakes in XWR is very likely due to the stress release and influence of pore pressure.

As it happens, our two types of earthquakes are roughly divided by the HYF: The dip-slip earthquakes locate in the reservoir area, while the strike-slip ones locate in the sediment basin. This may support the theory of water diffusion effect on stress state: in the water reservoir area, the tectonic stress is modified by pore pressure change from water diffusion. In the sediment basin, the local stress does not change that much, so strike-slip earthquakes still dominate.

6. Discussion

6.1. RTS in XWR

More than 90 reservoir-triggered seismicity (RTS) has been reported worldwide (e.g., Kariba in Zambia-Zimbabwe, Oroville in the U.S., Xinfengjiang in China, and Koyna in India; Gupta, 2002). XWR is one of the rare reservoirs that has triggered M6.1 earthquakes and has ongoing seismicity for more than 50 years. This makes it an ideal location to study the RTS. Comparison between XWR and other reservoirs shall also provide important information for our understanding of RTS.

Our results in this study suggest that current earthquakes in XWR mainly locate at 5–10-km depth. Investigation of historical earthquakes in XWR (Figure 13) clearly shows that they gradually migrate from shallow depth to deeper depth, especially at the first 5 years after the impoundment. The XFJ network for earthquake monitoring did not change much during the 1960s and 1980–2012 in both location and number (eight to nine stations), and after 2012, station number increased to 14. We believe that the time change for earthquake depth was not affected much by station distribution.

Talwani (1997) pointed out that the “protracted seismicity,” which continues for several years, even decades after impoundment, is a coupled poroelastic response to lake level fluctuation. Roeloffs (1988) calculated the frequency (Ω) of stress and pore pressure changes by reservoir load and define it as

$$\Omega = \omega L^2 / 2C \quad (1)$$

where ω is the loading frequency, L is the width of the reservoir, and C is the diffusion coefficient.

Equation (1) suggests that the frequency of earthquakes is governed by the water level change cycle. We examined this phenomena by comparing the Xinfengjiang water level, seismicity rate, and earthquake distribution over 40 years (Figure 14). The water level change of XWR has two obvious cycles. One is annual cycle (ω_1) with the water elevation changes (H1) to be about 10 m, and the other one is 5 years cycle (ω_2) with the lake level changes (H2) of 20–30 m. Meanwhile, earthquake number seems also to have dominating periods at ~5 years. The annual cycle of earthquakes is not obvious, which may suggest that longer cycle with greater water level change has more effect on the occurrence of earthquakes in XWR.

There have been some simulations on the effect of XWR water loading (e.g., Wang et al., 1976). Cheng et al. (2012) incorporated different faults and lithology in XWR area and calculated Columbus stress

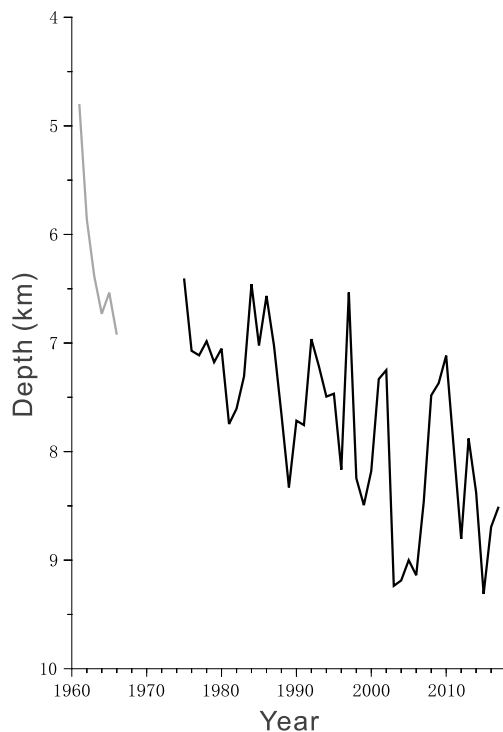


Figure 13. Average annual depth distribution of earthquakes from 1960 to 2016 in XWR. Earthquake depths of early years (gray line) are modified from Wang et al. (1976) and Ding et al. (1983), and the depths after 1975 (black line) are from earthquake catalog of Guangdong Earthquake Agency.

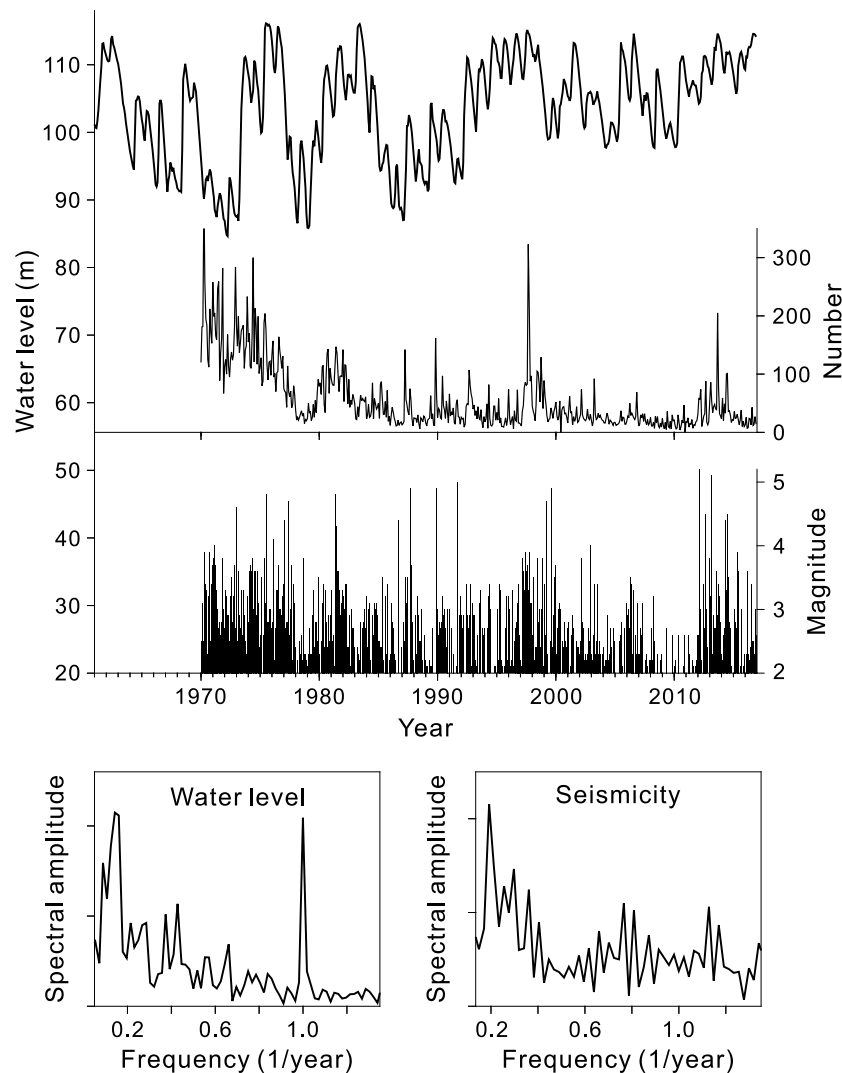


Figure 14. (top) The water level change, number of earthquakes with magnitude greater than 1, and earthquakes distribution of XWR as a function of time. For simplicity, we only plot earthquakes of magnitude greater than 2 in distribution figure. (bottom) Spectrums of water level (left) and earthquake number (right). The long time change cycle (~5 years) of water in XWR is correlated with seismicity rate change.

change in Xingfengjiang area from a 3-D model. They tested five models, and each model includes five different rock types in the reservoir area. The range of diffusion coefficients varies from 0.2 to 6.2 m^2/s . Their results suggest that stress increase on faults and reservoir area is about 0.7–3 kPa, depending on diffusion coefficient. The accumulated strain energy can only account for ~1% of the energy of the M6.1 earthquake; thus, the stress change from water loading should not be the main reason for the M6.1 earthquake. However, the water loading and diffusion may play an important role in triggering the main shock and keep working on generating numerous smaller protracted earthquakes.

Combining the above results, the earthquake mechanism dichotomy distribution, (Figure 12), and the correlation of V_p/V_s with V_s (V_p) in the fractures/faults, we conclude that water plays an important role in triggering protracted seismicity in XWR. Water level fluctuation cycle and amplitude may control earthquake occurrence frequency. Meanwhile, water penetrates into fractures, increases pore pressure, and modifies stress state and thus change the earthquake type and make the earthquake migrate gradually to deeper depth. Of course, we do not exclude effect of the tectonic settings (such as faults and rock hydrochemical properties) in XWR, but water does take advantage of the geology in XWR to shape the seismicity of this area.

6.2. Comparison to Koyna-Warna Water Reservoir

The Koyna-warna reservoir in India is one of the mostly studied RTS sites in the world. As another typical example of protracted seismicity, it shares many similarities with the XWR, such as the dam height, seismicity activity after impoundment, and the focal mechanisms of earthquakes (Bhattacharya, 2007; Rao & Shashidhar, 2016; Shashidhar et al., 2011). For example, both reservoirs have triggered M6 earthquakes within several years after impoundment, and numerous earthquakes continue to happen till today, including tens of M4 ones. Both Xinfengjiang and Koyna reservoir have more dip-slip earthquakes. They also have large-amplitude cyclical change in the lake level, as well as corresponding earthquake occurrence frequency (Talwani, 1997; this study).

However, both structure and seismicity in Xinfengjiang and Koyna-warna area have differences. Although the upper crustal structures of the two reservoirs show low V_s and high V_p/V_s in fracture areas, XWR area also shows correlated V_s and V_p change, while Koyna-warna reservoir shows anticorrelated V_s and V_p change. Moreover, earthquake depth in XWR migrates gradually to deeper depth and currently concentrates at 5–10-km depth. On the contrary, earthquakes in Koyna-warna reservoir still spread from near surface to more than 10 km from south to north (Dixit et al., 2014; Gupta, 2002; Rao & Shashidhar, 2016). Third, the distribution of earthquake type of XWR has dichotomy pattern in and outside reservoir area, but Koyna-warna reservoir earthquakes do not have such a pattern. Finally, the earthquakes in XWR have a dominated cycle of 5 years, but Koyna-warna has no obvious cycle. This may be because XWR has two water fluctuation cycles of 5 years and 1 year, while Koyna has only an annual cycle.

The similarities may form the similar reservoir dimension and water fluctuation time and magnitude. However, the water fluctuation cycles, the underground structures, and tectonic stress in the two reservoir areas are not the same. Xinfengjiang has a more fractured structure in granite blocks, while Koyna-warna has a more dominated fracture across the whole region (e.g., Catchings et al., 2015). The properties of the rocks may cause different water diffusion, and with different pore pressure changes inside the fractures, the velocity- and earthquake-type distribution may also be different.

7. Conclusions

In this study, we inverted upper crustal V_p , V_s structures and earthquake locations and focal mechanisms in XWR area. We have successfully obtained fine upper crust structures that have never been resolved before, in which low-velocity and high V_p/V_s structures appear clearly underneath the major fault systems, including a deep fracture along northwest-southeast directions. The earthquakes locate around high V_p/V_s regions, suggesting that the nucleation positions of the earthquakes are from the periphery, not the center of fractures. Our results also show more dip-slip earthquakes than strike-slip ones, which are roughly divided by the HYF at the east side of Xinfengjiang reservoir. Although we confirm that the local tectonic stress and the crustal structure in this area control the occurrence of earthquakes in XWR area, water does play an important role, as manifested in the gradual migration of earthquakes to deeper depth, and spatiotemporal changes of faulting types.

Because of the distribution of the seismic stations, in this study, we only investigate structures and earthquake mechanisms in the SE part of the reservoir. More studies in terms of the NW part of the reservoir may provide complementary information to better understand the Xinfengjiang Water Reservoir tectonic structure and earthquakes.

References

- Aki, K., & Lee, W. H. K. (1976). Determination of three-dimensional velocity anomalies under a seismic array using P-arrival times from location earthquakes: 1. A homogeneous initial model. *Journal of Geophysical Research*, *81*(23), 4381–4399. <https://doi.org/10.1029/JB081i023p04381>
- Awad, M., & Mizoue, M. (1995). Tomographic inversion for the three-dimensional seismic velocity structure of the Aswan region, Egypt. *Pure and Applied Geophysics*, *145*(1), 193–207. <https://doi.org/10.1007/bf00879494>
- Bhattacharya, S. N. (2007). Moment tensor solutions and triggering environment for earthquakes in Koyna-Warna water reservoirs region, India. *Pure and Applied Geophysics*, *164*(5), 909–928. <https://doi.org/10.1007/s00024-007-0199-2>
- Catchings, R. D., Dixit, M. M., Goldman, M. R., & Kumar, S. (2015). Structure of the Koyna-Warna Seismic Zone, Maharashtra, India: A possible model for large induced earthquakes elsewhere. *Journal of Geophysical Research: Solid Earth*, *120*, 3479–3506. <https://doi.org/10.1002/2014JB011695>

Acknowledgments

We thank the Editor, the Associate Editor, Xiaowei Chen, and another anonymous reviewer for their constructive comments and suggestions. The manuscript benefits a lot from them. This work is supported by the Strategic Priority Research Program (B) of Chinese Academy of Sciences (grant XDB18000000), National Science Foundation of China (41774053), NSFC/RGC Joint Research Scheme (projects N_CUHK418/15 and N_CUHK430/16), CUHK-University of Manchester Research Fund (project 4930227), HKSAR Research Grant Council GRF grants 14313816 and 14305617, CUHK Faculty of Science, and research grant of State Key Laboratory of Isotope Geochemistry (Guangzhou Institute of Geochemistry, Chinese Academy of Sciences) (SKLabiG-KF-16-03). The figures in this paper are generated by GMT (Generic Mapping Tool; Wessel & Smith, 1998). Seismic waveforms and water level data were obtained from Guangdong Earthquake Agency (<http://www.gddzj.gov.cn/dizhenshuju/dzshuju.asp>).

- Cheng, H. H., Zhang, H., & Zhu, B. J. (2012). Finite element investigation of the poroelastic effect on the Xinfengjiang reservoir-triggered earthquake (in Chinese). *Science China Earth Sciences*, 55(12), 1942–1952. <https://doi.org/10.1007/s11430-012-4470-8>
- Ding, Y., Pan, J., Xiao, A., Shen, L., Ma, H., & Miao, W. (1983). Tectonic environment of reservoir induced earthquakes in the Xinfengjiang reservoir area (in Chinese). *Seismology and Geology*, 5(3), 63–74.
- Ding, Y., Zeng, X., & Chen, Y. (1982). The aftershock activities of induced earthquakes in the Xinfengjiang reservoir areas (in Chinese). *Seismology and Geology*, 4(1), 23–30.
- Dixit, M. M., Kumar, S., Catchings, R. D., Suman, K., Sarkar, D., & Sen, M. K. (2014). Seismicity, faulting, and structure of the Koyna-Warna seismic region, western India from local earthquake tomography and hypocenter locations. *Journal of Geophysical Research: Solid Earth*, 119, 6372–6398. <https://doi.org/10.1002/2014JB010950>
- Feng, R. (1977). On the variations of the velocity ratio before and after the Xinfengjiang reservoir impounding earthquake of M 6.1 (in Chinese). *Chinese Journal of Geophysics*, 20(3), 211–221.
- Gritto, R., & Jarpe, S. P. (2014). Temporal variations of V_p/V_s -ratio at The Geysers geothermal field, USA. *Geothermics*, 52, 112–119. <https://doi.org/10.1016/j.geothermics.2014.01.012>
- Gritto, R., Romero, A. E., & Daley, T. M. (2004). Results of a VSP experiment at the Resurgent Dome, Long Valley caldera, California. *Geophysical Research Letters*, 31, L06603. <https://doi.org/10.1029/2004GL019451>
- Guo, G., & Feng, R. (1992). The joint inversion of 3-D velocity structure and source parameters in Xinfengjiang reservoir (in Chinese). *Chinese Journal of Geophysics*, 35(03), 331–342.
- Guo, G., Liu, T., Qin, N., & Chen, L. (2004). Analysis on small-earthquake composite fault plane solutions from 1961 to 1999 in Xinfengjiang reservoir area (in Chinese). *Acta Seismologica Sinica*, 26(3), 261–268.
- Gupta, H. K. (2002). A review of recent studies of triggered earthquakes by artificial/water reservoirs with special emphasis on earthquakes in Koyna, India. *Earth-Science Reviews*, 58(3–4), 279–310. [https://doi.org/10.1016/S0012-8252\(02\)00063-6](https://doi.org/10.1016/S0012-8252(02)00063-6)
- Hardebeck, J. L., & Shearer, P. M. (2002). A new method for determining first-motion focal mechanisms. *Bulletin of the Seismological Society of America*, 92(6), 2264–2276. <https://doi.org/10.1785/0120010200>
- Haskell, N. A. (1964). Total energy and energy spectral density of elastic wave radiation from propagating faults. *Bulletin of the Seismological Society of America*, 54(6A), 1811–1841.
- Huang, T., & Yang, M. (2001). Preliminary study on polarization of S-wave of Xinfengjiang earthquakes (in Chinese). *South China Journal of Seismology*, 21(4), 22–26.
- Moos, D., & Zoback, M. D. (1983). In situ studies of velocity in fractured crystalline rocks. *Journal of Geophysical Research*, 88(B3), 2345–2358. <https://doi.org/10.1029/JB088iB03p02345>
- Nur, A. (1972). Dilatancy, pore fluids, and premonitory variations of t_s/t_p travel times. *Bulletin of the Seismological Society of America*, 62(5), 1217–1222.
- Nur, A., & Simmons, G. (1969). The effect of saturation on velocity in low porosity rocks. *Earth and Planetary Science Letters*, 7(2), 183–193. [https://doi.org/10.1016/0012-821X\(69\)90035-1](https://doi.org/10.1016/0012-821X(69)90035-1)
- Pan, J., & Xiao, A. (1982). The preliminary study of seismic structures and their characteristic activity in Xinfengjiang reservoir area (in Chinese). *Seismology and Geology*, 4(2), 53–58.
- Rao, N. P., & Shashidhar, D. (2016). Periodic variation of stress field in the Koyna–Warna reservoir triggered seismic zone inferred from focal mechanism studies. *Tectonophysics*, 679, 29–40. <https://doi.org/10.1016/j.tecto.2016.04.036>
- Rawlinson, N., Kool, M. D., & Sambridge, M. (2006). Seismic wavefront tracking in 3D heterogeneous media: Applications with multiple data classes. *Exploration Geophysics*, 37(4), 322–330. <https://doi.org/10.1071/eg06322>
- Roeloffs, E. A. (1988). Fault stability changes induced beneath a reservoir with cyclic variations in water level. *Journal of Geophysical Research*, 93(B3), 2107–2124. <https://doi.org/10.1029/JB093iB03p02107>
- Sethian, J. A. (2001). Evolution, implementation, and application of level set and fast marching methods for advancing fronts. *Journal of Computational Physics*, 169(2), 503–555. <https://doi.org/10.1006/jcph.2000.6657>
- Shashidhar, D., Rao, N. P., & Gupta, H. (2011). Waveform inversion of broad-band data of local earthquakes in the Koyna–Warna region, western India. *Geophysical Journal International*, 185(1), 292–304. <https://doi.org/10.1111/j.1365-246X.2011.04935.x>
- Shearer, P. M. (1988). Cracked media, Poisson's ratio and the structure of the upper oceanic crust. *Geophysical Journal International*, 92(2), 357–362. <https://doi.org/10.1111/j.1365-246X.1988.tb01149.x>
- Shen, C., Chang, C., Chen, H., Li, T., Hueng, L., Wang, T., et al. (1974). Earthquakes induced by reservoir impounding and their effect on Hsinfengkiang dam. *Scientia Sinica*, 17(2), 239–272.
- Talwani, P. (1997). On the nature of reservoir-induced seismicity. *Pure and Applied Geophysics*, 150(3–4), 473–492. <https://doi.org/10.1007/s000240050089>
- Vavryčuk, V. (2014). Iterative joint inversion for stress and fault orientations from focal mechanisms. *Geophysical Journal International*, 199(1), 69–77. <https://doi.org/10.1093/gji/ggu224>
- Waldhauser, F., & Ellsworth, W. L. (2000). A double-difference earthquake location algorithm: Method and application to the northern Hayward fault, California. *Bulletin of the Seismological Society of America*, 90(6), 1353–1368. <https://doi.org/10.1785/0120000006>
- Wang, M., Yang, M., Hu, Y., Li, Z., Chen, Y., Jin, Y., & Feng, R. (1976). Mechanism of the reservoir impounding earthquakes at Xinfengjiang and a preliminary endeavor to discuss their cause (in Chinese). *Chinese Journal of Geophysics*, 19(1), 1–17.
- Wei, B., Chen, P., Li, F., & Huan, H. (1991). Focal mechanisms and tectonic stress field of the Xinfengjiang earthquakes (in Chinese). *Acta Seismologica Sinica*, 13(4), 462–470.
- Wessel, P., & Smith, W. H. F. (1998). New, improved version of generic mapping tools released. *Eos, Transactions American Geophysical Union*, 79(47), 579–579. <https://doi.org/10.1029/98EO00426>
- Yang, H. (2015). Recent advances in imaging crustal fault zones: A review. *Earthquake Science*, 28(2), 151–162. <https://doi.org/10.1007/s11589-015-0114-3>
- Yang, H., Li, Z., Peng, Z., Ben-Zion, Y., & Vernon, F. (2014). Low velocity zones along the San Jacinto Fault, Southern California, from body waves recorded in dense linear arrays. *Journal of Geophysical Research: Solid Earth*, 119, 8976–8990. <https://doi.org/10.1002/2014JB011548>
- Yang, H., & Zhu, L. (2010). Shallow low-velocity zone of the San Jacinto fault from local earthquake waveform modeling. *Geophysical Journal International*, 183(1), 421–432. <https://doi.org/10.1111/j.1365-246X.2010.04744.x>
- Yang, Z., Liu, B., Wang, Q., Zhao, C., Chen, Z., & Zhang, X. (2013). Tomographic imaging of the upper crustal structure beneath the Xinfengjiang reservoir area (in Chinese). *Chinese Journal of Geophysics*, 56(4), 1177–1189. <https://doi.org/10.6038/cjg20130413>
- Ye, X., Huang, Y., Hu, X., & Liu, J. (2013). Location of the Dongyuan Ms 4.8 earthquake sequence of Guangdong and 3D P-wave velocity structure in and around source region (in Chinese). *Acta Seismologica Sinica*, 35(6), 809–819.

- Zang, S. (1983). The effect of infiltrating of water and mechanism and characteristics of earthquakes in Xinfengjiang reservoir (in Chinese). *Seismology and Geology*, 5(2), 59–69.
- Zhang, H. (2003). Double-difference seismic tomography method and its applications (PhD thesis). Madison: University of Wis. Madison.
- Zhou, L., Xie, J., Shen, W., Zheng, Y., Yang, Y., Shi, H., & Ritzwoller, M. H. (2012). The structure of the crust and uppermost mantle beneath South China from ambient noise and earthquake tomography. *Geophysical Journal International*, 189(3), 1565–1583. <https://doi.org/10.1111/j.1365-246X.2012.05423.x>
- Zhu, L., & Ben-Zion, Y. (2013). Parametrization of general seismic potency and moment tensors for source inversion of seismic waveform data. *Geophysical Journal International*, 194(2), 839–843. <https://doi.org/10.1093/gji/ggt137>
- Zhu, L., & Helmberger, D. V. (1996). Advancement in source estimation techniques using broadband regional seismograms. *Bulletin of the Seismological Society of America*, 86(5), 1634–1641.
- Zhu, L., & Rivera, L. A. (2002). A note on the dynamic and static displacements from a point source in multilayered media. *Geophysical Journal International*, 148(3), 619–627. <https://doi.org/10.1046/j.1365-246X.2002.01610.x>